INTERNATIONAL JOURNAL FOR NUMERICAL METHODS IN FLUIDS
Int. J. Numer. Meth. Fluids 2005; **47**:543–559
Published online 17 December 2004 in Wiley InterScience (www.interscience.wiley.com). DOI: 10.1002/fld.829

Numerical realization for analysis of real flows by integrating computation and measurement

Toshiyuki Hayase*,†, Keisuke Nisugi and Atsushi Shirai

Institute of Fluid Science, Tohoku University, Japan

SUMMARY

In this paper, we deal with a numerical realization, which is a numerical analysis methodology to reproduce real flows by integrating numerical simulation and measurement. It is difficult to measure or calculate field information of real three-dimensional unsteady flows due to the lack of an experimental field measurement method, as well as of a way to specify the exact boundary or initial conditions in computation. Based on the observer theory, numerical realization is achieved by a combination of numerical simulation, experimental measurement, and a feedback loop to the simulation from the output signals of both methods. The present paper focuses on the problem of how an inappropriate model or insufficient grid resolution influences the performance of the numerical realization in comparison with ordinary simulation. For a fundamental flow with the Karman vortex street behind a square cylinder, two-dimensional analysis is performed by means of numerical realization and ordinary simulation with three grid resolutions. Comparison of the results with those of the experiment proved that the feedback of the experimental measurement significantly reduces the error due to insufficient grid resolution and effectively reduces the error due to inappropriate model assuming two-dimensionality. Copyright © 2004 John Wiley & Sons, Ltd.

KEY WORDS: numerical realization; numerical simulation; experiment; feedback; observer; Karman vortex street

1. INTRODUCTION

Numerical simulation and experiment are essential tools in flow analysis, but not appropriate to reproduce real flows exactly. It is apparent that there is no measurement method with which it is possible to obtain complete information on general time-dependent three-dimensional flows. This fact also explains why exact simulation is impossible for real flows whose exact boundary and initial conditions are not available. This paper deals with a numerical analysis

*Correspondence to: Toshiyuki Hayase, Institute of Fluid Science, Tohoku University, 2-1-1 Katahira, Sendai 980-8577, Japan.
†E-mail: hayase@ifs.tohoku.ac.jp

Contract/grant sponsor: Grant-in-aid for Scientific Research; contract/grant numbers: 10650157, 11555053

Received 15 August 2003
Accepted 18 August 2004

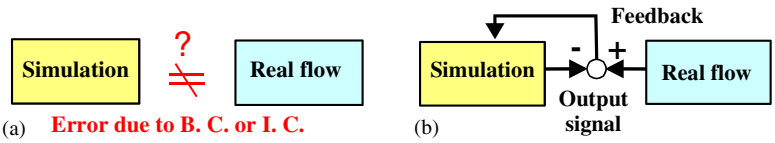

Figure 1. Comparison between real flow, simulation, and numerical realization: (a) simulation and real flow; (b) numerical realization.

methodology to reproduce real flows by integrating numerical simulation and experimental measurement.

In order to clarify the purpose of this study, it is useful to classify the objectives of numerical simulation into two categories: analysis in artificial conditions and analysis in real conditions. The first important and powerful use of simulations is analysis performed under conditions arbitrarily specified by analysts. Investigation over a wide variety of parameter values reveals the structure or the internal relationship of the phenomena. This is, of course, an essential process in design problems, and thus, numerical simulation has been taking the place of the experimental approach to resolve design problems in many fields.

The second important objective of numerical simulations is analysis performed under real conditions, in which the goal is to obtain information on the internal states of real phenomena. This is essential in control problems in a wide sense. As stated above, this is not a trivial issue for field problems because of the difficulty in determining the boundary and initial conditions. In a 3-D flow problem with 1000^3 grid points, for example, the number of boundary conditions to be specified is of the order of 1000^2. It is obviously unrealistic to determine all the boundary values by measurement.

We have proposed a concept of *numerical realization* [1], which is defined as a numerical simulation with a mechanism to include information of real phenomena in order to perform simulations under real conditions. The observer [2] in dynamical system theory is the key concept to solve this problem. For observable and controllable finite-dimensional linear dynamical systems, a theoretical framework has been established to design an observer, which derives the whole state variables from observation of a finite number of output signals [3]. As shown in Figure 1(a), error is inevitably introduced to the flow simulation through the boundary condition (B.C.) or the initial condition (I.C.). Figure 1(b) explains numerical realization based on the concept of the observer. First, a finite number of measurable output signals are defined in the domain of simulation, and a number of input signals are defined on the boundary or in the domain. The feedback law is determined to reduce the discrepancy of the output signals between the real flow and the simulation. If the feedback is designed properly, all the state variables of the simulation converge to those of the real flow.

Existing studies of the observer applied for flow problems are mostly limited to linear problems of relatively small order. The Kalman filter, which is a kind of observer for stochastic systems, has been successfully applied to estimate velocity profiles of a transient flow through a pipe for the application of time-dependent flow measurement [4]. Recently, many studies have been done on the estimation of flow fields in relation to flow control problems. Turbulent flow in the near-wall region has been estimated through proper orthogonal decomposition (POD) [5] or linear predictive filtering [6]. A theoretical study of the observer for the whole turbulent flow field in a square duct has been made by the present author [7]. In that work, a standard flow simulation algorithm was used for the mathematical model of the flow. The

feedback controller in the observer was designed to compensate the boundary condition of the simulation based on the estimation error between output signals of the computational and the experimental results, the latter of which is represented by the DNS result. The estimation error in the axial velocity at the grid points on a cross-section is fed back to the pressure boundary condition based on the simple proportional control law. Appropriate choice of the feedback gain significantly accelerates the convergence of the iterative calculation and reduces the error in the downstream region of the output measurement plane. As the first case of integration of computation and experiment in a real system, the *hybrid wind tunnel* was constructed by integrating an experimental wind tunnel and a supercomputer through a high speed network [8]. Numerical realization was carried out with this equipment for the flow with the Karman vortex street behind a square cylinder. Pressure measurement on the cylinder wall was fed back to the numerical simulation showing that the numerical realization reproduces the Karman vortex appearing in a real flow. Especially, exact synchronization of the oscillations obtained by computation and experiment is a specific feature of the hybrid wind tunnel.

As the potential of the above-mentioned numerical realization method in simulating real flows has been ascertained, fundamental properties of the methodology should be further investigated. The present paper focuses on the problem of how an inappropriate model and insufficient grid resolution influence the performance of the present numerical realization method. It is common to begin a numerical analysis in a rather restricted but simple condition, such as an assumption of two-dimensionality of a relevant flow. The question to be investigated is whether the feedback of measurement data in the numerical realization can reduce the effect of the model error in comparison with ordinary simulations. The second question is whether the effect of incomplete grid resolution can be reduced by the feedback action. In order to investigate these problems, numerical realization and ordinary simulation are performed with three grid systems of different resolutions, and all the results, including the experimental one, are compared with each other.

In Section 2 of the paper, the governing equations and numerical procedures for computation of the 2-D channel flow with a square object are presented. Inclusion of the measurement in the computation is explained in detail. In Section 3, results for the flow with the Karman vortex street are compared between the numerical realization, the ordinary numerical simulation for three grid resolutions and the experiment. Section 4 of the paper presents the conclusions of the work.

2. FORMULATION

The real flow field to be investigated is illustrated in Figure 2. A square cylinder with a 30×30 mm cross section is placed in the channel with a length of 2510 mm and a 200×200 mm cross section. The two-dimensional Cartesian co-ordinate system (x, y) is defined on the middle plane of the channel as shown in the figure. As the flow condition, the mean velocity is set at $U_0 = 0.6$ m/s (mean velocity at the origin) with a Reynolds number $Re(= U_0 D/\nu,\ D = 30$ mm: the width of the cylinder) of 1200. Non-uniformity of the mean velocity distribution at $x = 0$ is 3.5%. In this condition, the Karman vortex with a shedding frequency of 2.75 Hz was observed in the experiment.

In the numerical realization, a two-dimensional domain with a length of 600 mm is defined as the shaded region in Figure 2. Governing equations for incompressible and viscous fluid

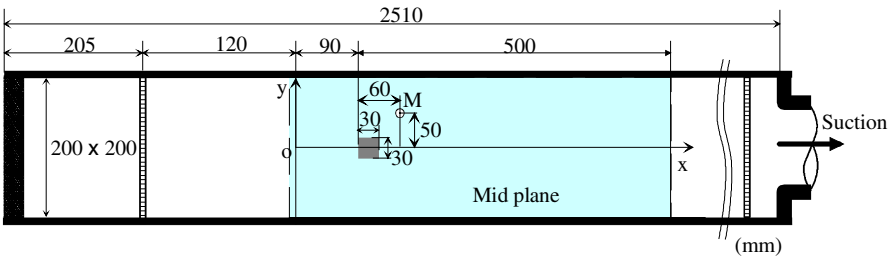

Figure 2. Geometry and coordinate system.

flow are the Navier–Stokes equation

$$\rho\left(\frac{\partial \mathbf{u}}{\partial t}+(\mathbf{u}\cdot\mathrm{grad})\mathbf{u}\right)=-\mathrm{grad}\,P+\mu\nabla^2\mathbf{u}+\mathbf{f} \tag{1}$$

and the equation of continuity

$$\mathrm{div}\mathbf{u}=0 \tag{2}$$

where **f** in Equation (1) is the artificial body force corresponding to the feedback signal in the numerical realization as described later in this section. Parallel flow with the uniform velocity U_b is applied at the upstream boundary,

$$u(y)=U_\mathrm{b},\ v(y)=0 \text{ at } x=-D/3 \tag{3}$$

where the upstream boundary velocity U_b is treated as the feed-forward input variable in the numerical realization. The downstream boundary condition is free stream. The no-slip condition is applied on the solid walls. All velocity components are initially set at null in the whole domain.

The governing equations are discretized with the finite volume method on the uniformly spaced staggered grid system and are solved with the algorithm similar to the SIMPLER method of Patankar [9]. As the main feature of the present scheme, (1) a consistently reformulated QUICK scheme is applied to the convective terms [10] and (2) the second order implicit scheme is used for the time derivative terms [11]. Details of the scheme are given in a previous paper [12].

Three grid systems of different resolutions, i.e. $N_x\times N_y=60\times 21$ (Grid A), 120×42 (Grid B), and 240×82 (Grid C), are used for the numerical realization and the ordinary simulation. A time step of 1 ms, the same as the sampling time of the pressure measurement, was confirmed to be sufficiently small for the present calculations. Conditions used in the calculation are summarized in Table I.

In the numerical realization, measurement of the real flow is supplied to the numerical simulation to compensate for the differences between the real flow and the computation. Since we focus on the Karman vortex originating from the cylinder, the output signal to be measured is defined as the pressure on the both sides of the cylinder relative to the stagnation pressure (see Figure 3),

$$\begin{pmatrix}P^*_{AS}\\ P^*_{BS}\end{pmatrix}=\begin{pmatrix}P^*_A-P^*_S\\ P^*_B-P^*_S\end{pmatrix} \tag{4}$$

Table I. Computational condition.

Grid system	Grid A	Grid B	Grid C
Domain $L_x \times L_y$		$20D \times 6.67D$	
Grid points $N_x \times N_y$	60×21	120×42	240×82
Grid spacing $h_x \times h_y$	$D/3 \times D/3$	$D/6 \times D/6$	$D/12 \times D/12$
Time step h_t		0.001 s	
Width of cylinder D		0.03 m	
Mean velocity U_0		0.6 m/s	
Reynolds number Re		1200	

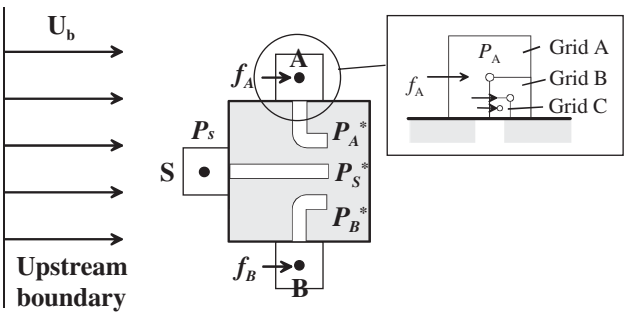

Figure 3. Details of the square cylinder.

where the asterisk represents experimental values. Corresponding variables P_{AS} and P_{BS} are defined using the computational results. Note that the location of pressure evaluation in the computation is different between the grid systems as shown in Figure 3.

The artificial body force **f** in Equation (1) is calculated in proportion to the difference between the output signals in the experiment and those in the calculation. The corresponding forces f_A and f_B are applied to the control volumes A and B (Figure 3), respectively, in the x-direction momentum equation.

$$\begin{pmatrix} f_A \\ f_B \end{pmatrix} = -KA_{\mathrm{C}} \begin{pmatrix} P_{AS} - P^*_{AS} \\ P_{BS} - P^*_{BS} \end{pmatrix} \tag{5}$$

where K denotes the feedback gain (non-dimensional), and A_{C} the cross-sectional area of the control volume. The velocity component u is accelerated or decelerated by the feedback of Equation (5) at the upstream boundary of the pressure control volumes. As a result, the pressure error in the pressure equation decreases in these control volumes.

The uniform flow velocity of the real flow is estimated from the pressure measurement with the Pitot tube law [13], and fed forward to the upstream boundary velocity U_{b} of the simulation through the first-order low pass filter as

$$T_c \frac{\mathrm{d}U_{\mathrm{b}}}{\mathrm{d}t} + U_{\mathrm{b}} = K_e \sqrt{\frac{2P^*_m}{\rho}} \tag{6}$$

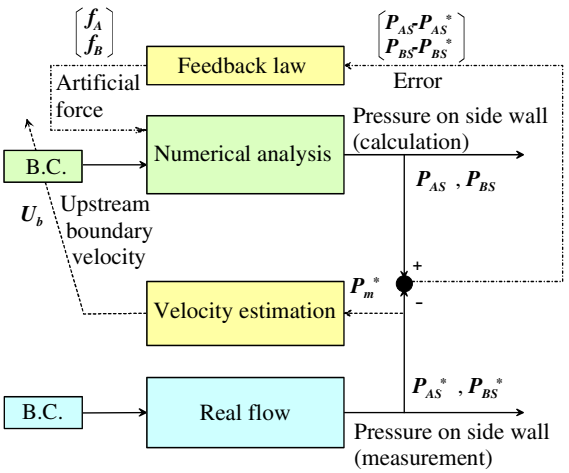

Figure 4. Block diagram of numerical realization for Karman vortex.

where T_c is the time constant of the filter, K_e is the velocity coefficient (non-dimensional), and P_m^* is the dynamic pressure estimated as

$$P_m^* = -\frac{P_{AS}^* + P_{BS}^*}{2} = P_S^* - \frac{P_A^* + P_B^*}{2} \tag{7}$$

Figure 4 shows the block diagram of the numerical realization. The pressure error on both sidewalls is fed back to the artificial forces f_A and f_B, and the estimated uniform flow velocity U_b is fed forward to the upstream boundary velocity condition.

3. RESULTS AND DISCUSSION

Three parameters in designing the numerical realization, namely, the feedback gain K, the velocity coefficient K_e, and the time constant T_c, are so determined that the estimated velocity u at the monitoring point M ($(x, y) = (5D, 1.67D)$, see Figure 2) best agrees with that of the experiment. The results are given as

$$K = 1.8,\ K_e = \begin{cases} 0.54\ \text{(grid A)} \\ 0.56\ \text{(grid B)}, \\ 0.60\ \text{(grid C)} \end{cases} \quad T_c = 0.3\ \text{[s]} \tag{8}$$

It is noted that only the parameter K_e depends on the grid system since the computational result is very sensitive to this parameter in comparison with the other parameters [8].

The results for one of the output signals, i.e. P_{AS}, the pressure at point A on the sidewall relative to the stagnation pressure, are compared in Figure 5. In Figures (a)–(c) corresponding to grids A–C, the left-hand side shows the results of the ordinary simulation and the right-hand side shows those of the numerical realization. Figure 5(d) shows the experimental result.

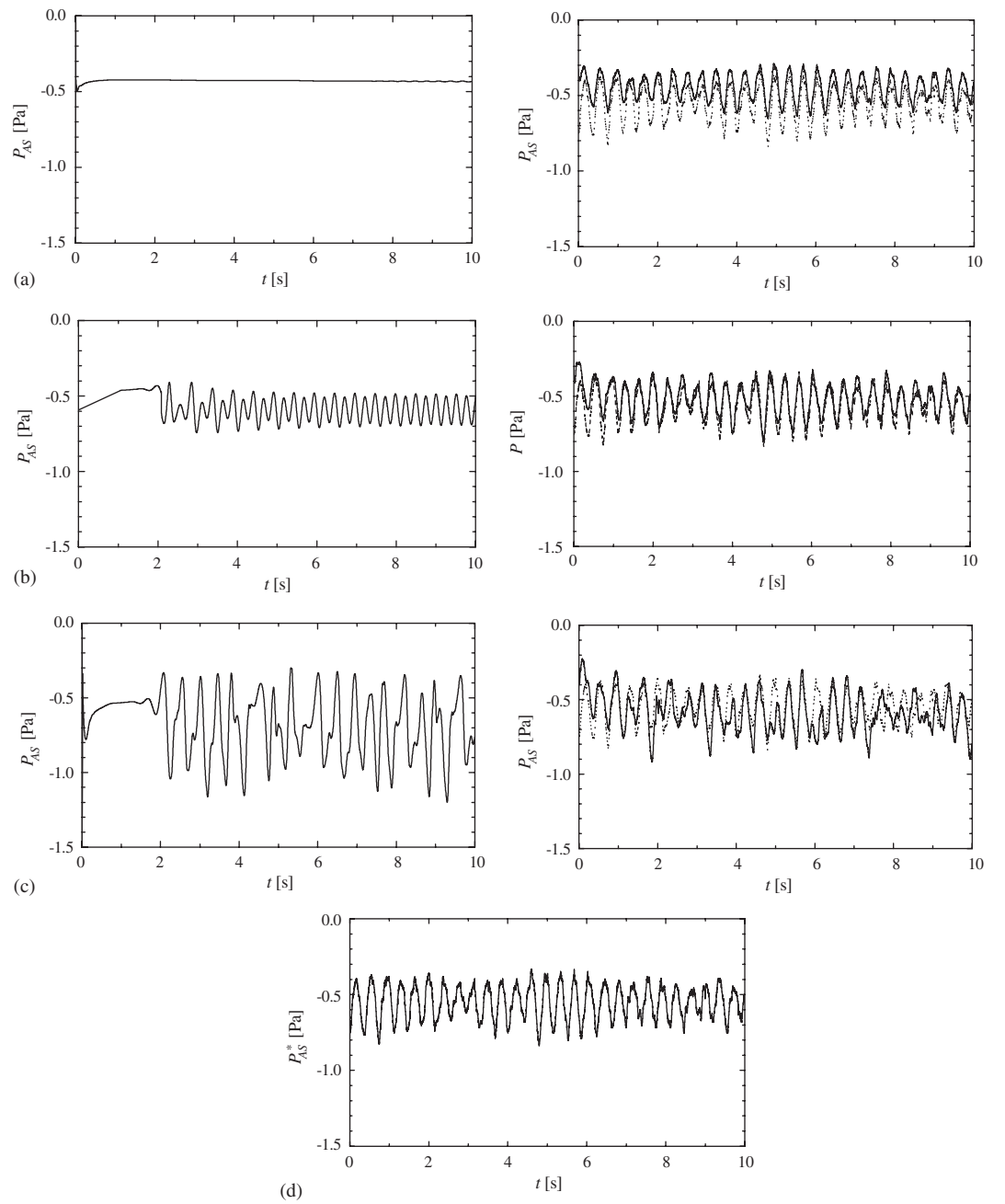

Figure 5. Comparison of pressure at point A relative to the stagnation pressure. Left: ordinary simulation; right: numerical realization (solid line) and experiment (dotted line); bottom: experiment: (a) grid A; (b) grid B; (c) grid C; (d) experiment.

The ordinary simulation on the left-hand side shows a variety of results, but none of these resembles the experimental result. With the coarse grid A, oscillation is almost invisible. The result of grid B shows a sinusoidal oscillation after the transient, and that of the fine grid C shows an irregular oscillation of large amplitude. It is noted that the result of the ordinary simulation with grid C is almost convergent with the grid refinement, which is confirmed by comparison with the result for the grid system which is twice as fine. In contrast, results of the numerical realization on the right-hand side show far better agreement with the experimental results (dotted lines, identical to Figure 5(d)) than do the results of the ordinary simulations. This justifies the appropriateness of the feedback algorithm defined in the former section for reducing the discrepancy of the pressure at points A and B.

A feedback signal for the numerical realization, or the artificial force applied to control volume A, is plotted in Figure 6. It is noted that the amplitude of the feedback signal shows a degree of inappropriateness of the model in reproducing the relevant flow. In the result of the coarse grid A, the force oscillates in the intervals $t = 0$–2 [s] and 4.5–6.5 [s] in which the amplitude of the computed pressure is smaller than that of the experiment (see Figure 5(a)). Variation of the feedback signal is rather small in other time intervals in which the calculated pressure agrees with the experimental values. Fluctuation of the force is rather small in the result of the medium grid B, implying a good agreement between the computation and experiment. Amplitude of the feedback force variation increases again with the fine grid C.

The velocity u at the monitoring point M is compared in Figure 7. As already mentioned, the parameters for the numerical realization are determined based on the agreement of this velocity component with the experimental values. Results of the ordinary numerical simulation on the left-hand side show variation similar to those of the pressure in Figure 5. They reveal a poor agreement with the experimental results shown in Figure 5(d). The best agreement with the experiment is achieved in the numerical realization with the coarse grid A. Irregularity of the velocity oscillation increases with grid refinement on the results of the numerical realization in the right-hand side. Degradation of the results obtained with the grid refinement is ascribed to inappropriateness of the two-dimensional model as discussed later in this section.

The amplitude of the FFT analysis for the velocity component u at monitoring point M is compared in Figure 8. In order to remove the effect of the transient state, data is processed between 10 and 30 s. It is apparent that the oscillation frequency obtained by the ordinary simulation on the left-hand side is very different from that of the experiment (dotted lines). Oscillation frequency of the numerical realization in the right-hand figures exactly agrees with that of the experiment. The best agreement of the frequency component profile is attained in the result of the coarse grid A.

Table II compares the results of the ordinary simulation and the numerical realization for the time-averaged velocity u_{mean}, the rms of the velocity perturbation u'_{rms}, and the peak frequency of the oscillation at monitoring point M. Data is processed between 10 and 30 s and presented as the ratio to the experimental values. Results for the mean velocity u_{mean} of the ordinary simulation (OS) converges to that of the experiment due to improvement of the grid resolution. However, the velocity perturbation u'_{rms} increases to a value larger than the experimental value with the grid refinement. The peak frequency for the ordinary simulation also does not converge to the experimental one. These discrepancies are ascribed to the inappropriateness of the two-dimensional model. A similar undesirable grid convergence property also appears in the numerical realization (NR) for u'_{rms}. However, the numerical realization represents better agreement with the experimental results than the ordinary simulation. The peak frequency for

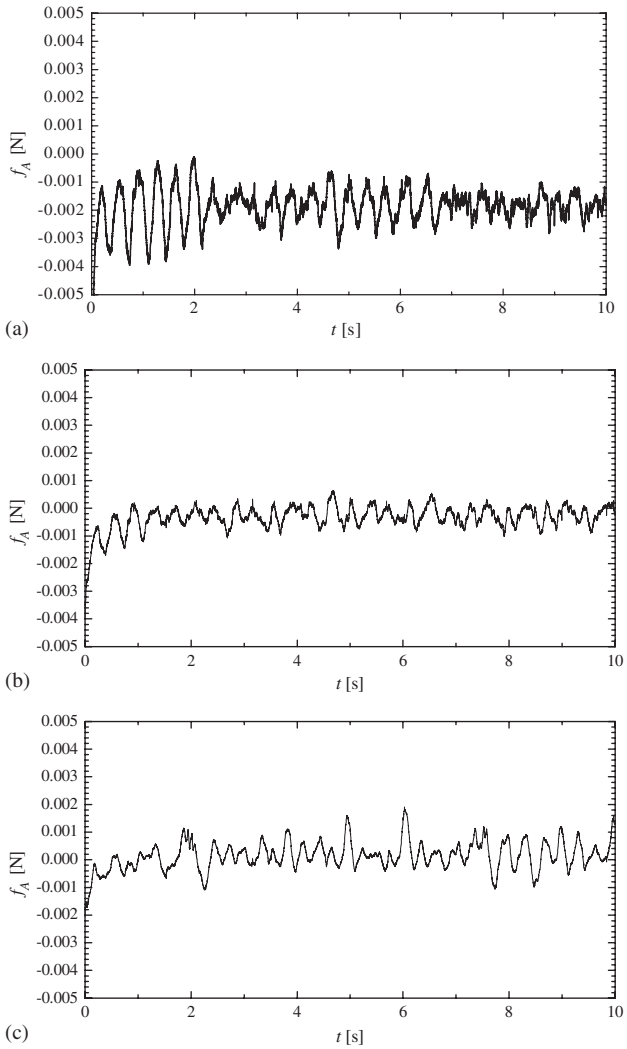

Figure 6. Force applied at point A in numerical realization: (a) grid A; (b) grid B; (c) grid C.

the numerical realization, on the other hand, exactly agrees with that of the experiment for all three grid systems. These results mean that the error introduced by an inappropriate model is effectively reduced by the feedback incorporated in numerical realization.

Distributions of the mean velocity u_{mean} are compared in Figure 9. Results of the ordinary simulation are given on the left-hand side. A stretched wake behind the cylinder in the result of the coarse grid A is much improved in the results of grids B and C, showing good agreement with that of the experiment (Figure (d)). Results of the numerical realization on the right-hand side agree with those of the experiment even with coarse grid A.

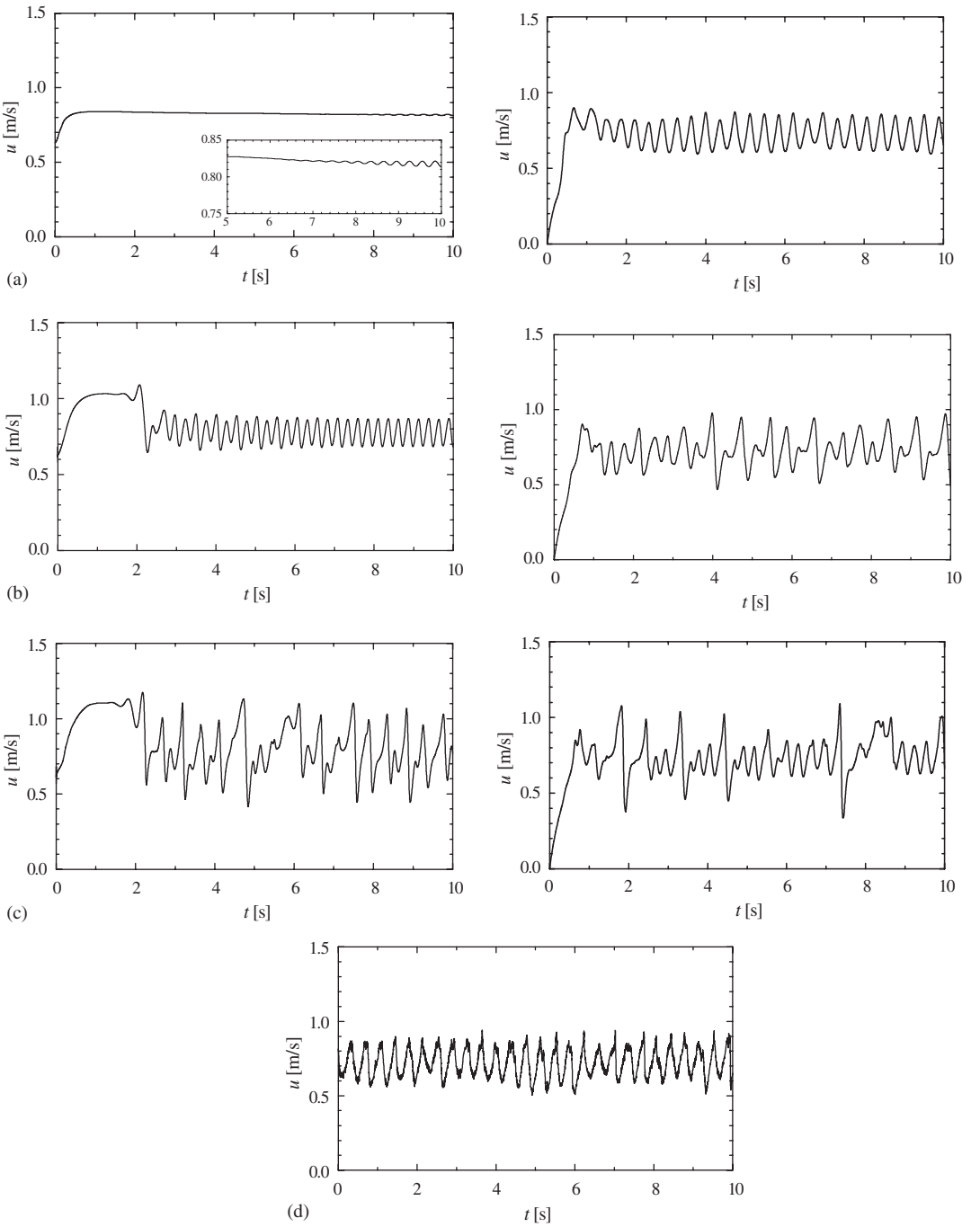

Figure 7. Comparison of velocity u at monitoring point M. Left: ordinary simulation; right: numerical realization; bottom: experiment: (a) grid A; (b) grid B; (c) grid C; (d) experiment.

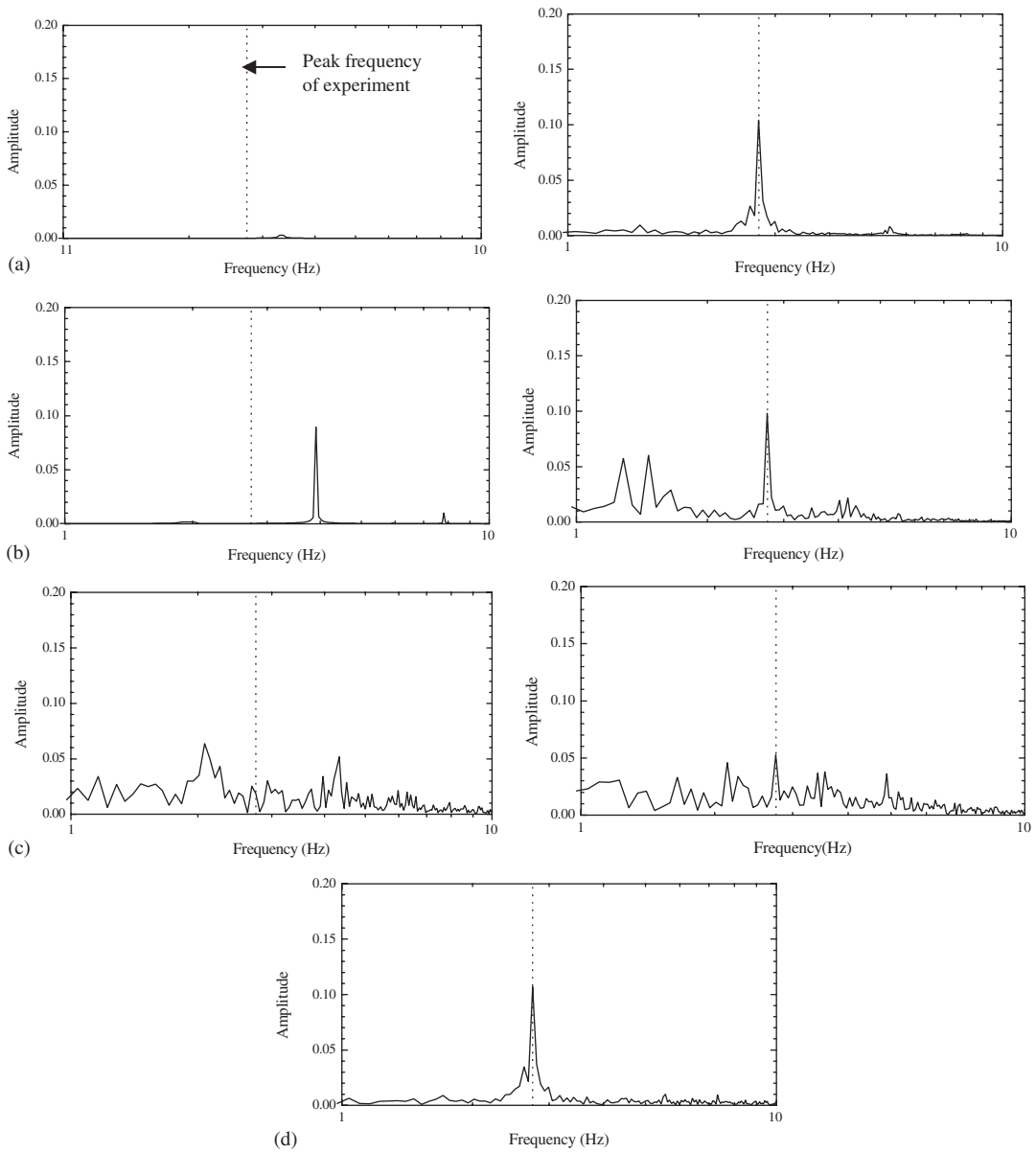

Figure 8. Comparison of FFT analysis for velocity u at monitoring point M. Left: ordinary simulation; right: numerical realization; bottom: experiment: (a) grid A; (b) grid B; (c) grid C; (d) experiment.

The rms values of the perturbation velocity u'_{rms} are compared in Figure 10. The result of the experiment in Figure 10(d) shows large velocity perturbation due to the Karman vortex shedding behind downstream corners of the cylinder. Results of the ordinary simulation on the left-hand side show a variety of distributions. The coarse grid A does not reproduce

Table II. Comparison between numerical realization and ordinary simulation based on the results at monitoring point M. Results are evaluated relative to those of the experiment. OS: ordinary simulation; NR: numerical realization; e_{OS}, e_{NR}: error for OS and NR, respectively.

Grid system		Grid A	Grid B	Grid C
u_{mean}	OS	1.13	1.08	1.05
	NR	1.01	1.03	1.01
	e_{NR}/e_{OS}	0.08	0.4	0.2
u'_{rms}	OS	0.03	0.66	1.53
	NR	0.89	1.14	1.31
	e_{NR}/e_{OS}	0.1	0.4	0.6
Peak frequency	OS	1.20	1.42	0.76
	NR	1.00	1.00	1.00
	e_{NR}/e_{OS}	0.0	0.0	0.0

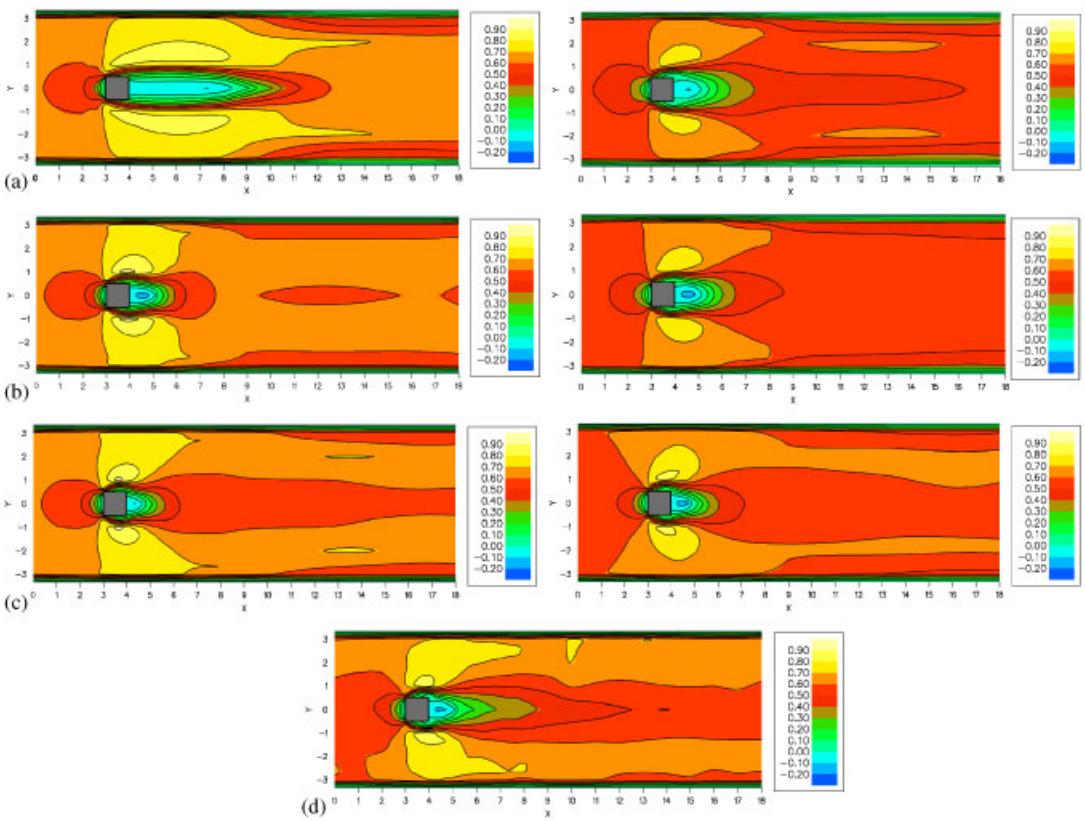

Figure 9. Mean velocity u_{mean}. Left: ordinary simulation; right: numerical realization; bottom: experiment: (a) grid A; (b) grid B; (c) grid C; (d) experiment.

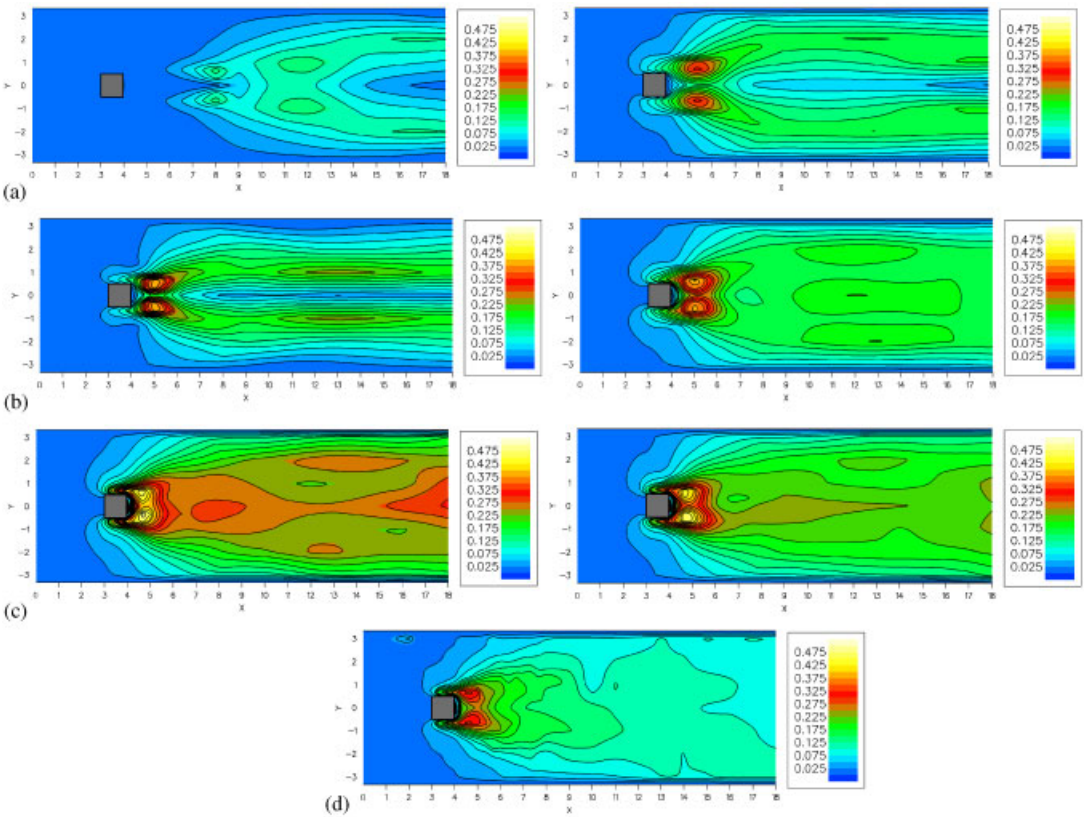

Figure 10. Perturbation velocity u'_{rms}. Left: ordinary simulation; right: numerical realization; bottom: experiment: (a) grid A; (b) grid B; (c) grid C; (d) experiment.

the velocity fluctuation near the cylinder but shows a region with small perturbation far downstream of the cylinder. The result of the moderate grid B shows the best agreement with the experimental result among the results of the ordinary simulation. The fine grid C results in a much larger amplitude of velocity fluctuation than the experiment. The numerical realization shows better results than the ordinary simulation for all grid systems. Similar to the mean velocity distribution, the most significant improvement of the perturbation velocity is seen for the results with the coarse grid A.

Reproducibility with the ordinary simulations and the numerical realizations mentioned above is quantified by the error with respect to the experiment. Figure 11 compares the distributions of the error for the mean velocity u_{mean}. In the result of the ordinary simulation with the coarse grid A on the left-hand side of Figure 11(a), a large error occurs behind the cylinder. The result of the numerical realization with the same grid on the right-hand side reveals a substantial reduction of the error behind the cylinder but some increase near the walls in the downstream region. The same trend is seen for the other two grids, grids B and C, but the difference between the ordinary simulation and the numerical realization is smaller than in the case of the coarse grid A.

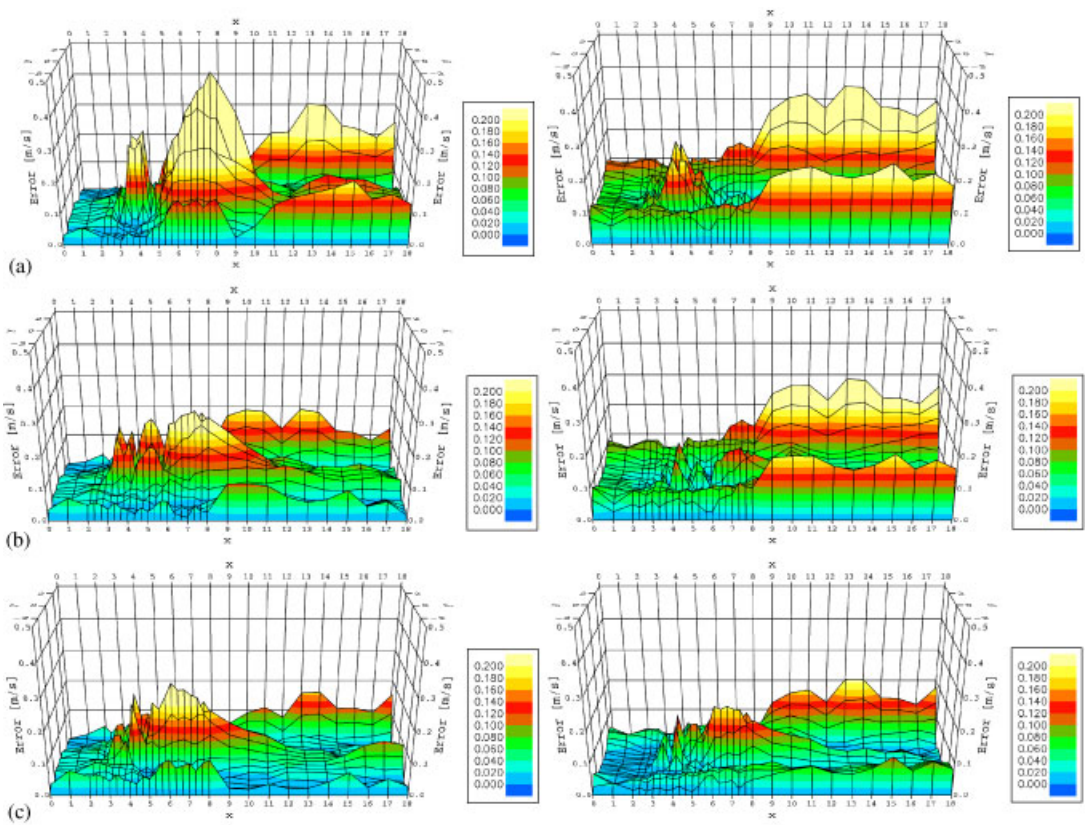

Figure 11. Error in mean velocity u_{mean} from experiment. Left: ordinary simulation; right: numerical realization: (a) grid A; (b) grid B; (c) grid C.

Comparison of the error in the rms value of the perturbation velocity u'_{rms} in Figure 12 reveals qualitatively the same result as the case of the mean velocity, but the influence of the grid resolution appears more clearly. In the coarse grid A, a large error of the ordinary simulation beside or behind the cylinder (left-hand figure) is drastically reduced in the corresponding result of the numerical realization (right-hand figure). Due to the inappropriateness of the two-dimensional model, the results of the ordinary simulation and the numerical realization with the fine grid C are inferior to the corresponding results with the medium grid B. It is apparent that the numerical realization results in smaller error than the ordinary simulation for all three grid systems.

The results of the above discussion can be summarized as follows. In the results of the ordinary simulation, large error for the coarse grid A is mainly ascribed to an insufficient grid resolution, while that of the fine grid C is mainly due to an inappropriate two-dimensional model. Significant improvement of reproducibility in the coarse grid A means that the numerical realization improves the grid convergence of the solution. It should be noted that computational load for the feedback process is negligibly small in comparison with that of

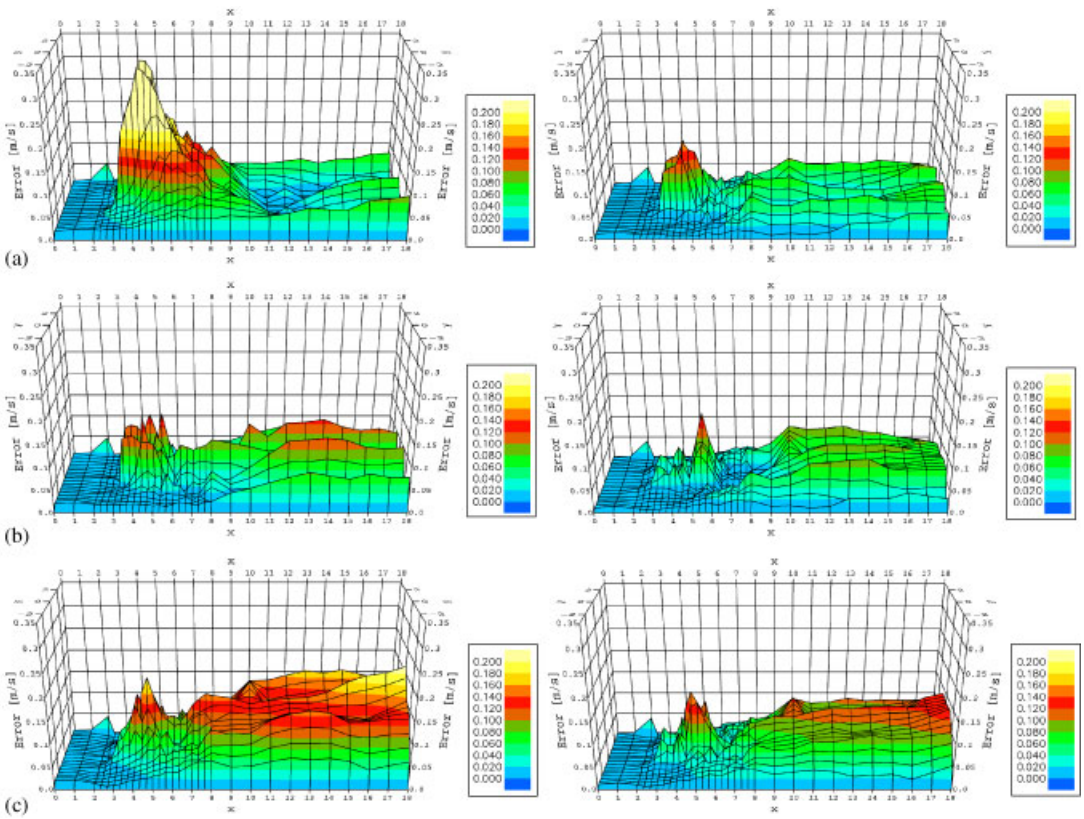

Figure 12. Error in perturbation velocity u'_{rms} from experiment. Left: ordinary simulation; right: numerical realization: (a) grid A; (b) grid B; (c) grid C.

the flow solver. Reduction of the error for the fine grid C, on the other hand, means that numerical realization also reduces the influence of an inappropriate model.

Finally, Figure 13 shows some examples of the streakline pattern obtained with the experiment, the numerical realization with the coarse grid A, and the ordinary simulations with the coarse grid A and the fine grid C. The streakline pattern of the numerical realization in Figure 13(b) is very similar to that of the experiment in Figure 13(a). It is noted that the oscillation phase of the numerical realization exactly agrees with that of the experiment due to the feedback effect. The streakline pattern of the ordinary simulations with the coarse and fine grids in Figures 13(c) and (d) both show poor results with smaller or larger fluctuation of the streaklines in comparison with the experiment.

4. CONCLUSIONS

This study constitutes a fundamental study on numerical realization, which is a numerical analysis methodology to reproduce real flows by integrating numerical simulation and mea-

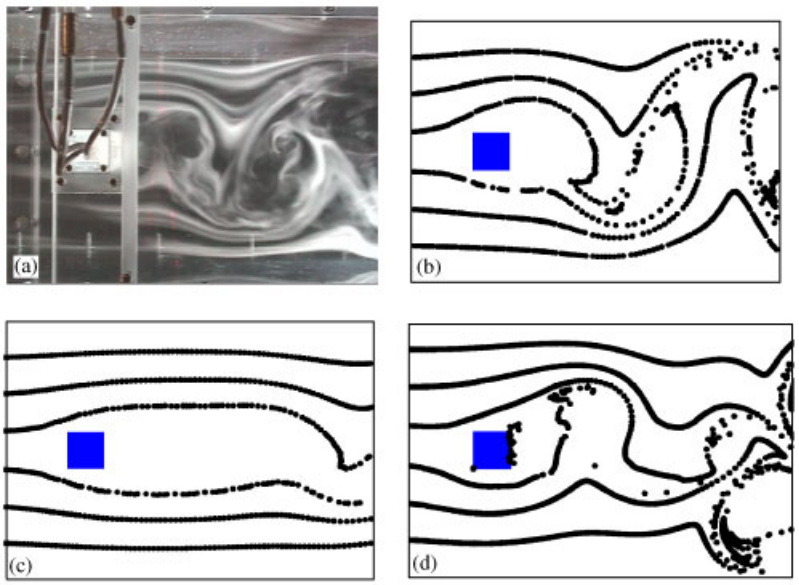

Figure 13. Comparison of streakline patterns. $t = 17.93$ s: (a) experiment; (b) numerical realization (grid A); (c) ordinary simulation (grid A); (d) ordinary simulation (grid C).

surement. For a fundamental flow with the Karman vortex street behind a square cylinder, numerical realization is achieved by a combination of numerical simulation, experimental measurement, and a feedback loop to the simulation from the output signals of both the methods. Especially, focus of this study was on the influences of an inappropriate model and an insufficient grid resolution on the performance of the numerical realization in comparison with the ordinary simulation. Two-dimensional analysis was performed with three grid systems for numerical realization and ordinary simulation. Because of the inappropriateness of the two-dimensional model, results of the ordinary simulation for the frequency and the amplitude of the velocity fluctuation did not converge to those of the experiment. Comparison of the simulation results with those of the experiment proved that the feedback of the experimental measurement significantly reduces the error due to the insufficient grid resolution in the coarse grid and effectively reduces the error in the fine grid due to the inappropriate model.

ACKNOWLEDGEMENTS

The authors express their sincere thanks to technicians T. Hamaya, T. Watanabe, Y. Fushimi, and K. Asano of the Institute of Fluid Science, Tohoku University for construction of the experimental apparatus and graduate student S. Takeda for his patient experimental measurement. The authors also gratefully acknowledge support received from a Grant-in-aid for Scientific Research (#10650157, 11555053). The calculations were performed using SGI ORIGIN 2000 at the Advanced Fluid Information Research Center, Institute of Fluid Science, Tohoku University.

REFERENCES

1. Hayase T, Nisugi K, Shirai A. Numerical realization of flow field by integrating computation and measurement. In *Proceedings of Fifth World Congress on Computational Mechanics* (WCCM V), Mang HA, Rammerstorfer FG, Eberhardsteiner J (eds). Paper-ID: 81524, 2002; 1–12.
2. Luenberger DG. *Introduction to Dynamic Systems*: *Theory*, *Models*, *and Applications*. Wiley: New York, 1979.
3. Misawa EA, Hedrick JK. Nonlinear observers: a state-of-the-art survey. *Journal of Dynamic Systems*, *Measurement*, *and Control Transactions* (ASME) 1989; **111**:344–352.
4. Uchiyama M, Hakomori K. Measurement of Instantaneous flow rate through estimation of velocity profiles. *IEEE Transaction of Automatic Control* 1983; **AC-28**:380–388.
5. Podvin B, Lumley J. Reconstructing the flow in the wall region from wall sensors. *Physics of Fluids* 1998; **10**:1182–1190.
6. Amonlirdviman K, Breuer K. Linear predictive filtering in a numerically simulated turbulent flow. *Physics of Fluids* 2000; **12**:3221–3228.
7. Hayase T, Hayashi S. State estimator of flow as an integrated computational method with feedback of online experimental measurement. *Journal of Fluids Engineering Transactions* (ASME) 1997; **119**:814–822.
8. Nisugi K, Hayase T, Shirai A. Fundamental study of hybrid wind tunnel integrating numerical simulation and experiment in analysis of flow field. *JSME International Journal* 2004; **B-47**:593–604.
9. Patankar SV. *Numerical Heat Transfer and Fluid Flow*. Hemisphere: Washington, DC, New York, 1980.
10. Hayase T, Humphrey JAC, Greif R. A consistently formulated QUICK scheme for fast and stable convergence using finite-volume iterative calculation procedures. *Journal of Computational Physics* 1992; **98**:108–118.
11. Fletcher CAJ. *Computational Techniques for Fluid Dynamics*, vol. 1. Springer: Berlin, 1988; 302.
12. Hayase T. Monotonic convergence property of turbulent flow solution with central difference and QUICK scheme. *Journal of Fluids Engineering Transactions* (ASME) 1999; **121**:351–358.
13. Benedict RP. *Fundamentals of Pipe Flow*. Wiley: New York, 1980.

